A bio-inspired self-burrowing probe in shallow granular materials

Ningning Zhang [a]; Yuyan Chen [b, *]; Alejandro Martinez [b]; Raul Fuentes [a]

[a] *Institute of Geomechanics and Underground Technology, RWTH Aachen University, 52074 Aachen, Germany*

[b] *Department of Civil and Environmental Engineering, University of California Davis, Davis, CA 95616, United States*

*Corresponding author at: Department of Civil and Environmental Engineering, University of California Davis, Davis, CA 95616, United States. E-mail address: yych@ucdavis.edu (Chen)

ABSTRACT

Bio-inspired strategies have been used in recent years to solve engineering problems in geotechnics. Inspired by the dual-anchor locomotion mechanism of razor clams, researchers are developing a new generation of self-burrowing probes for a wide range of applications such as site exploration and sensor deployment. Due to inherent complexities of the bio-inspired self-burrowing mechanism, the interaction between the probe and soil is not fully understood, hindering the development of physical prototypes. In this study, a model based on the discrete element method (DEM) is used to prove feasibility, study and optimize the self-burrowing process of a probe. The probe burrows in a gravity-settled chamber filled with a scaled discrete analogue of a silica sand. A stepwise methodology including essential anchor expansion, tip penetration and anchor retraction behaviors is proposed to model the self-burrowing process. Tip oscillation is introduced to reduce penetration resistance, which enables efficient burrowing through continuous cycles. However, the reduction strategy of soil resistance consumes more than 50% of the total work done by the entire self-burrowing cycle. Micromechanical observations such as contact force network and particle displacement field are provided to clearly visualize the interaction between the soil and the probe. Whilst the total energy necessary to penetrate is larger than an equivalent constant rate penetration, the feasibility of such probe is numerically proven.

KEYWORDS: bio-inspiration, self-burrowing probe, discrete element method, granular materials

MANUSCRIPT submitted to *Journal of Geotechnical and Geoenvironmental Engineering*

Authors: N. Zhang et al.

List of Notations

D_{50} particle mean size

D_C chamber diameter

D_r relative density

D_S original shaft diameter

D_{SA} shaft anchor diameter

D_{TA} tip anchor diameter

d_c probe tip cone diameter

ER_S shaft expansion ratio

ER_T tip expansion ratio

F_n normal contact force at particle scale

$F_{N,z}$ neck vertical force

F_{SA} shaft anchor capacity

$F_{S,bot,z}$ vertical force on shaft bottom surface

$F_{S,r}$ actual shaft radial force

$F_{S,r,inc}$ shaft radial force increment

$F_{S,r,target}$ target shaft radial force achieved during expansion

$F_{S,r,tot}^{t}$ resultant shaft radial force

$F_{S,z}$ shaft vertical (anchor) force

$F_{S,z,max}$ maximum shaft vertical (anchor) force

$F_{Tcone,x}$ tip cone force along x-axis direction

$F_{Tcone,z}$ tip cone vertical force

$F_{Tcyl,top,z}$ vertical force on tip cylinder top surface

$F_{Tcyl,z}$ tip cylinder vertical force

$F_{Tcyl,z,max}$ maximum tip cylinder vertical force

$F_{Tcyl,r,}$ radial force measured on tip cylinder

$F_{Tcyl,r,target}$ target radial force on tip cylinder achieved during expansion

F_{TA} tip anchor capacity

$F_{top,z}$ vertical force on the probe top

g gravitational acceleration

G shear modulus

H_C Chamber height

h burrowing depth

h_E height of probe embedment

h_N height of probe neck

h_S height of probe shaft

h_{TCyl} height of probe tip cylinder

l_p probe length

m_p probe mass

m_S shaft mass

n number of load increments for shaft expansion

n_1, n_2 n_3, n_4 *and* n_5 scaling factors

n_p probe/particle size ratio

N particle number

Q_T tip resisting force during penetration

Q_S shaft resisting force during shaft retraction

r_1, r_2 rough model parameters

R_d chamber/probe diameter ratio

S_q surface roughness

t_1 tip oscillation time length

$v_{Tcyl,r}$ tip cylinder radial expansion velocity

$v_{S,r}$ shaft radial expansion velocity

$v_{S,r}{}^{t}$ shaft radial expansion velocity at time t

$v_{S,r}{}^{t+\Delta t}$ shaft radial expansion velocity at time (t+Δt)

v_p tip penetration velocity

v_{SC} shaft contraction velocity

v_{SR} shaft retraction velocity

v_{TC} tip contraction velocity

v_{TO} oscillation velocity of tip point along one single vertical plane

W_{CRP} work done by constant rate penetration

W_{SC} work done by shaft contraction

W_{SE} work done by shaft expansion

W_{SR} work done by shaft retraction

W_{TC} work done by tip contraction

W_{TE} work done by tip expansion

W_{TO} work done by tip oscillation

W_{tot} total self-burrowing work

W_{TP} work done by tip penetration

σ_z vertical stress

μ friction coefficient of soil

μ_p friction coefficient of probe

δ contact overlap

δ_1, δ_2 rough model parameters

v Poisson's ratio

Δt time step

$\Delta\rho_{shaft}$ shaft penetration distance in one burrowing cycle

$\Delta\rho_{tip}$ tip penetration distance in one burrowing cycle

Abbreviations

CPT	cone penetration test
CF	constant force
CR	constant radius
CV	constant velocity
DEM	discrete element method
ILC	incremental load control
PRM	particle refinement method
PSD	particle size distribution
QSP	quasi-static penetration
REM	radius expansion method
SC	shaft contraction
SE	shaft expansion
SPT	standard penetration test
SR	shaft retraction
TC	tip contraction
TE	tip expansion
TP	tip penetration
TO	tip oscillation

1 Introduction

Strategies inspired by biology are multifunctional, redundant, robust and efficient and thus they have been applied in geotechnics to facilitate engineering advances and solve engineering problems (Martinez et al., 2021). In the last decade, ongoing research in bio-inspired geotechnics has emerged from four main areas: (a) snakeskin-inspired surfaces (O'Hara & Martinez, 2022; Martinez et al., 2019; Zhong et al., 2021); (b) root-inspired anchorage systems and foundations (Bengough & Mullins, 1990; Burrall et al., 2021; Mallett et al., 2018; Mickovski et al., 2011); (c) burrowing probes (Chen et al., 2021; Huang & Tao, 2020; Tao et al., 2020; Winter et al., 2014), and; (d) robotic excavation (Carotenuto et al., 2020; De Macedo et al., 2021; Frost et al., 2017).

In particular burrowing robots, strategies inspired by the dual-anchor locomotion of razor clams (Trueman, 1967), the peristaltic locomotion of earthworms (Dorgan, 2015), and the rotational growth mode of seed roots (Taylor et al., 2021) have been employed to develop a new generation of self-burrowing robotic probes (Tao et al., 2020; Winter et al., 2014). Relevant studies of self-burrowing probes include numerical modelling, cavity expansion analyses and laboratory testing (Borela et al., 2021; Chen et al., 2021; Huang & Tao, 2020; Martinez et al., 2020; Tang & Tao, 2022). In the future, self-burrowing robots could be used for site exploration, search and rescue, sensor deployment, inspection, monitoring, surveillance, transport, and construction purposes (Tao, 2021). These applications are expected not only on Earth but also on outer-space bodies such as Mars and the Moon.

Figure 1 illustrates the typical burrowing cycle of a razor clam employing a dual-anchor locomotion mechanism (Trueman, 1967), whose simplicity and efficiency have attracted particular attention for the development of self-burrowing probes. This mechanism cyclically alternates expansion and contraction of the back (shell) and front (foot) anchors to achieve forward movement. During a cycle, (i) the shell first expands to form an anchor to provide sufficient reaction force for the foot to (ii) penetrate further into the soil. Then, (iii) the foot expands and the shell contracts. In this stage, (iv) the foot acts as an anchor to drag the shell down into the soil. Inspired by this locomotion strategy, Winter et al. (2014) developed the '*RoboClam*' robot which uses a reduced amount of energy compared to what would be required quasi-statically pushing the probe into the soil. Soil fluidization is also used to aid in the burrowing with the Roboclam; however, field trials were only able to reach a depth of 0.3 m. Tao et al. (2019) and Tao et al. (2020) developed a self-burrow-out soft robot that uses cycles of longitudinal contraction and expansion. Borela et al. (2021) developed an earthworm-inspired robot which was tested in sands. Most of the tests in this study failed to self-burrow due to the limited length of the robot's anchor which resulted in insufficient mobilization of anchorage forces. The above studies highlight the challenges of developing self-burrowing robots or tools.

Researchers have performed numerical simulations to further understand the robot-soil interactions. For example, Huang & Tao (2020) used a discrete element method (DEM) model to study the influence zone created by the body expansion of razor clams, but the DEM model simplified the dual-anchor system of razor clams to only one shaft anchor, which created impractical self-burrowing. Chen et al. (2021, 2022a, 2022b) investigated the effects of different soil conditions and probe configurations on the performance of the self-penetration process of a bio-inspired probe using DEM models. However, the probe control strategy was simplified, likely leading to limitations in the modeling of the of soil-probe interactions. Martinez et al. (2020) proposed a cavity-expansion-theory method for modeling a self-penetrating bio-inspired probe. However, this method works only for vertical penetration and does not account for the interactions between periodic radial expansion and tip penetration. Indeed, a more versatile model employing more realistic self-burrowing mechanisms (e.g., dynamic and force-controlled) is still missing to achieve clear understanding of the soil-probe interaction.

In the following sections we describe the construction of a three-dimensional chamber filled with a calibrated discrete analogue of a representative silica sand. Then we describe the modeled self-burrowing probe and propose a basic methodology for modeling each step involved in the dual-anchor strategy through different mechanisms. These include oscillation of the tip to reduce penetration resistance and constant-force control of the back anchor to avoid loss of anchorage. The probe is finally able to burrow deeply into the soil after continuous self-burrowing cycles. The results presented cover both macroscale (e.g., penetration distance, mechanical work) and microscale (e.g., contact force chains between soil particles, particle displacement) variables that help explain the different interaction mechanisms occurring during locomotion and penetration.

2 Model construction

2.1 Chamber-related model details

2.1.1 Particle-based numerical model for Fontainebleau sand

Fontainebleau sand is a fine silica sand that has been extensively used in geotechnical research. Table 1 lists its physical properties. In this study, we use a discrete analogue of the natural material in a calibrated DEM model consisting of spherical particles in the DEM code PFC3D (Itasca, 2017). Particle rotation was fully restricted by fixing all the rotational degrees of freedom of particles to roughly mimic the effect of non-spherical particle shapes. This simplified approach can be traced back to Ting et al. (1989) and was successfully used in previous penetration work in granular materials (Arroyo et al., 2011; Calvetti et al., 2015; Zhang et al., 2021; Zhang et al., 2019).

The contact model developed by Otsubo et al. (2017) for rough particles was chosen. The model was developed based on the standard Hertzian model with the following characteristics: contacts between particles are assumed to be elasto-plastic; the slip behavior at contacts is defined by the friction coefficient μ; each contact presents non-linear stiffness controlled by the elastic properties of material particles, e.g., shear modulus G, and Poisson's ratio v. The developed model is able to more completely consider soil characteristics than the standard Hertzian model by incorporating measurable surface roughness S_q. Roughness is particularly relevant at small strain levels where deformation and breakage of asperities occur. This effect is described by a three-stage relationship between the normal force, F_n, and the normal displacement, δ, originated from the standard Hertzian model (Figure 2). The F_n-δ relationship describes three successive contact regimes (i.e., asperity-dominated, transitional, and Hertzian) separated by two points T1 and T2. δ_1 and δ_2 are model parameters that are a function of the particle roughness S_q:

$$\delta_1 = r_1 S_q \quad (1)$$

And,

$$\delta_2 = r_2 S_q \quad (2)$$

where r_1 and r_2 are model parameters. When S_q =0, the standard Hertzian relationship is recovered.

The calibrated parameters of the rough contact model for Fontainebleau sand are provided in Table 2 (Zhang et al., 2021). Wishing to use realistic material-based values, G was assigned as 32 Gpa and v as 0.19, which are appropriate values for SiO_2 according to industrial databases (Zhang et al., 2021). S_q was set as 0.6 μm, considered as a realistic roughness value for silica sand. The values of r_1 and r_2 were set as 0.05 and 5, respectively after calibration against the results of contact experiments on Leighton Buzzard Sand (LBS) fraction A reported by Nardelli & Coop (2019) as shown in Figure 3a. To further validate this set of parameters, DEM models using uncrushable spheres were run to capture the initial loading behaviour of high-pressure oedometer tests, using a 4 mm sided cube of frictionless rigid walls filled with 10,000 spherical particles (Figure 3b). Particle diameter ranged from 0.1 to 0.4 mm matching the particle size distribution (PSD) of Fontainebleau NE34 sand. Figure 3c shows a close match between the initial non-crushing loading stages measured in both the experiments and DEM models, successfully validating the calibrated parameters.

2.1.2 Chamber construction

A three-dimensional cylindrical chamber was constructed using wall elements. All the chamber walls were set to be frictionless. Geometrical model details can be found in Figure 4 and Table 3. Discrete elements filling up the chamber have the same contact properties and size distribution as those used for the particle assembly calibration shown in Figure 3. The particle sizes were upscaled applying five distinct scaling factors following the particle refinement method (PRM) (Ciantia et al., 2018; Huang & Tao, 2020; McDowell et al., 2012; Sharif et al., 2020). This method allows to achieve sufficient contacts between the particles and the probe whilst reducing the number of particles in the whole system. In detail, a scaling of 35 was used to multiply the particle sizes at the center of the chamber. Particles further away from the center were upscaled using factors with the central scaling multiplied by a uniform set of multipliers (1.5, 2.25, 2.7 and 3.24). That means the five scaling factors used from the center to the boundary are 35, 53, 79, 95 and 113, termed as n_1, n_2, n_3, n_4 and n_5, respectively. The multipliers (≤ 1.5) can effectively prevent particle migration between adjacent zones (McDowell et al., 2012). A specific dimensional configuration of the five zones was chosen as: the outermost ring and innermost zone have a greater dimension with 14 cm, while the intermediate three rings have smaller thicknesses acting as filter layers. The upscaling of particle sizes does not affect the overall response as the particle mechanical properties remain unchanged (McDowell et al., 2012).

The simulations are desired to initiate from the free ground surface to evaluate the self-burrowing performance of the probe at shallow depths. The radius expansion method (REM) was used to fill the chamber at the porosity of 0.40. Then, the top wall was deleted and gravity was applied to settle the soil mass until reaching equilibrium state. During gravity settling, the inter-particle friction was set to a relatively small value of 0.05 to attain a dense uniform sample with a clear vertical stress gradient induced by gravity (Figure 4b). At the bottom of the specimen, the vertical effective stress is 10.9 kPa, matching the stress level of a real soil column. This inter-particle friction to settle the soils was chosen balancing acceptable sample quality and computation time. Figure 4c shows a spatially uniform distribution of D_r owing to the specimen generation method employed in the simulations, and the average D_r value is 0.86. After equilibrium, the inter-particle friction coefficient was reset to the calibrated value (Table 1). All the chamber walls were fixed throughout simulations. In all simulations, a local damping of 0.05 (Cundall, 1987) was employed and no viscous damping was considered.

2.2 Probe-related model details

2.2.1 Bio-inspired probe

Inspired by the burrowing strategies of the razor clam, here we provide a feasibility study of a dual-anchor self-burrowing probe. Geometrical details of the probe are shown in Figure 5 and Table 4. The probe is composed of three connected segments: shaft, neck and tip. All the segments were created using rigid walls, which don't interact with each other.The tip consists of a cone with the apex angle of 60° and a cylinder that can expand to behave as an anchor. The diameter of the tip and neck d_c was selected as 3.56 cm in consistency with conventional cone penetration test (CPT) probe sizes and the height of the tip cylinder h_{Tcyl} was set equal to d_c. The neck height h_N is equal to its diameter and the shaft height is $5d_c$. An embedment extends into the shaft and has a length equal to the shaft length. *The shaft diameter D_S was enlarged to 1.05 times d_c to avoid repeated calculation of probe-particle contacts at the overlapping of the shaft and the embedment.* The shaft can expand to form another anchor with the soil to facilitate sufficient tip penetration distance during one burrowing cycle. To prevent particles from flowing into the probe, each probe segment was created with end caps whose diameter also changes as the sections are expanded during anchor deployment.

The total length of the probe is 24.4 cm, and therefore the ratio of probe length to tip diameter is 6.8. As reported by Martinez et al. (2020), this ratio falls into the normal range (2-9) of razor clam species. Also, the shaft anchor has a length of 4 times the tip diameter, fulfilling the requirement that anchor length should cover 2.0 to 4.5 times tip diameter to generate sufficient anchorage forces as determined by Martinez et al. (2020) using cavity expansion simulations. The probe mass m_p is 2.23 kg which was assumed to remain unchanged during the whole self-burrowing simulation including anchor expansion stages. The probe/particle diameter ratio n_p and chamber/probe diameter ratio R_d are two key factors influencing soil penetration results. In this study, the n_p in the central portion is 4.8 and the R_d is 20. Both values are higher than most of the values chosen in previous three-dimensional soil penetration studies as summarized by Chen et al. (2021). The contact model between probe and particles was also a simplified Hertz-Mindlin. The parameters for the probe were given in Table 2.

2.2.2 Methodology for a stepwise self-burrowing cycle

A stepwise self-burrowing methodology is designed following closely the locomotion mechanism of razor clams. As illustrated in Figure 6, one single self-burrowing cycle of the probe, following an initial penetration phase in which the probe is fully inserted into the sand material to reach the condition of mobilizing shaft friction, is completed in six individual steps. It is assumed that during each step, relevant segments move only with the motions specified in this section of the probe, while other motions of these segments and all motions of the other segments are restricted. The six steps are:

I. Shaft Expansion (SE)

To form the shaft anchor, the shaft expands radially under incremental load control (ILC) to reach a target force $F_{S,r,target}$. The expansion aims to provide sufficient reaction force for tip penetration in step TP. The load control allows gradual increase of the radial force with a relatively small loading increment $F_{S,r,inc}$. At each increment, the force is held constant until the shaft expansion rate is zero, similar to typical loading procedures of the pressuremeter test. After stabilization, new increments are applied to reach the target force. The shaft radial expansion velocity is updated using the following equation:

$$v_{S,r}{}^{t+\Delta t} = v_{S,r}{}^{t} + \frac{F_{S,r,tot}^{t}}{m_S}\Delta t \qquad (3)$$

where, $v_{S,r}{}^{t+\Delta t}$ and $v_{S,r}{}^{t}$ are the shaft radial velocities in all radial directions at time (t+Δt) and t, respectively, Δt is the time step, m_S is the shaft mass (1.57 kg), and $F_{S,r,tot}^{t}$ is the resultant radial force acting on the shaft:

$$F_{S,r,tot}^{t} = nF_{S,r,inc} - F_{S,r}^{t} \qquad n=1, 2, \ldots, [F_{S,r,target} / F_{S,r,inct}] \qquad (4)$$

Where, n is the number of load increments, and $F_{S,r}$ is the actual shaft radial force.

The use of force control algorithm enables the consideration of soil-robot interaction that can lead to a more realistic performance (Barasuol et al., 2018). This loading algorithm corresponds to the criterion *C1* in Figure 6.

Similar to the expansion limitations of animals due to muscular capacity, the probe also imposes a limit in shaft expansion ratio ER_S. The expansion magnitude is calculated as a ratio of the shaft anchor diameter D_{SA} and a limit value of 50% (*C2*) is adopted in consistency with that required in the pressurementer tests (Houlsby & Withers, 1988):

$$ER_S = \frac{D_{SA} - D_S}{D_S} \leq 50\% \qquad (5)$$

The expansion terminates in the case that one of the two criteria (*C1* or *C2*) is met. The actual shaft radial force $F_{S,r}$ may be smaller than $F_{S,r,target}$ if the *C2* criterion is triggered.

A slight upward movement of the shaft anchor is needed to mobilize its anchorage force to resist tip penetration in the next step. However, due to the motion restriction stated above, during tip penetration the shaft anchor does not displace in any direction. Therefore, we assume to use $F_{S,r}$ and the shaft friction coefficient to determine the anchor capacity (i.e., the maximum vertical anchor force $F_{S,z,max}$), which will be constantly compared with penetration resistance during TP:

$$F_{S,z,max} = \mu_p F_{S,r} \qquad (6)$$

II. Tip Penetration (TP)

With the help of the shaft anchor, the probe extends and pushes its neck and tip downwards for a distance of $\Delta\rho_{tip}$ with a constant velocity v_p. The vertical forces resisting penetration include $F_{N,z}$, $F_{Tcyl,z}$ and $F_{Tcone,z}$, which are vertical forces measured along the neck, tip cylinder and tip cone, respectively. To simplify expressions, these three resisting terms can be combined as one single soil resistance term Q_T:

$$Q_T = F_{N,z} + F_{Tcyl,z} + F_{Tcone,z} \qquad (7)$$

To balance resisting forces, the static shaft anchor force $F_{S,z}$, which is smaller than $F_{S,z,max}$, is mobilized as a reaction force. As a potential source of reaction force, the soil weight acting onto the shaft top surface $F_{top,z}$ is, however, not considered due to its negligible magnitude at the shallow depths modeled here.

Shaft anchor capacity F_{SA} is composed of the maximum vertical anchor force $F_{S,z,max}$ (Eq. 6) with the assistance of the probe's self-weight $m_p g$:

$$F_{SA} = \mu_p F_{S,r} + m_p g \qquad (8)$$

Where, g is the gravitational acceleration. Note that as stated before, it is assumed that the anchor does not displace to mobilize the anchor capacity, while the maximum anchorage force is mathematically calculated using Eq. 6. In this manner, the balance between the actual vertical anchorage force, which remains lower than its possible maximum value, and the soil resisting force is satisfied, as defined in the C3 criterion:

$$F_{SA} \geq Q_T \quad (9)$$

In addition, to constrain excessive penetration, another limiting condition *C4* is defined so that the penetration magnitude $\Delta\rho_{tip}$ cannot exceed d_c.

During penetration, a simple way to deal with the shaft anchor is to maintain its radius as constant, which can be described as constant radius *(CR)* condition. However, this strategy may not be able to provide sufficient anchorage for tip penetration. As demonstrated by Chen et al. (2021) and Chen et al. (2022), tip penetration causes a continuous reduction on shaft anchor force due to interactive effects between the tip and the shaft. Therefore, it is necessary to maintain the constant force (*CF*) of the shaft employing a servo control mechanism to enable tip penetration, which means the shaft continues to expand. Hence, the criterion *C2* needs to be re-activated to impose an expansion limit on the shaft anchor.

III. Tip Expansion (TE)

Similar to the shaft anchor expansion procedure, the tip cylinder is expanded to form another anchor using the ILC algorithm. The tip cone is not expanded as that would reduce the anchor effect due to vertical force generation at the cone. The expansion aims to achieve a target radial force of the tip anchor of $F_{Tcyl,r,target}$ (*C5*) which must enable successful shaft retraction in step V. Radial velocity algorithms similar to Eq. (3) & (4) are employed to update the tip radial velocity $v_{Tcyl,r}$. As can be seen from the criterion *C6*, a limit of 50% is also imposed to the tip expansion ratio ER_T, which is calculated from the tip anchor diameter D_{TA}:

$$ER_T = \frac{D_{TA} - d_c}{d_c} \quad (10)$$

The actual tip cylinder radial force $F_{Tcyl,r}$ may be smaller than $F_{Tcyl,r,target}$ if the *C6* criterion is triggered. $F_{Tcyl,r}$ is used to calculate the maximum vertical force of tip anchor $F_{Tcyl,z,max}$ that can be mobilized to resist shaft retraction in step V:

$$F_{Tcyl,z,max} = \mu_p F_{Tcyl,r} \quad (11)$$

IV. Shaft Contraction (SC)

The shaft is contracted back to its original size with a constant velocity v_{SC}, as defined in the criterion *C7*. Shaft contraction requires a smaller force compared with shaft expansion, enabling the feasibility of employing a much faster contraction rate than expansion (Table 5).

V. Shaft Retraction (SR)

The shaft is dragged downwards with a constant velocity v_{SR} until the shaft penetration distance $\Delta\rho_{shaft}$ is equal to $\Delta\rho_{tip}$ as defined in the criterion *C8*. At this point, the original probe length is recovered. The tip anchor capacity F_{TA} is composed of the maximum vertical force of the tip anchor $F_{Tcyl,z,max}$ (Eq. 11), vertical force at the tip anchor top surface $F_{Tcyl,top,z}$, and the probe self-weight $m_p g$. Thus, the expression of F_{TA} is written as:

$$F_{TA} = \mu_p F_{Tcyl,r} + F_{Tcyl,top,z} + m_p g \qquad (12)$$

During retraction, the shaft experiences soil resisting forces at both the shaft body and shaft bottom surface:

$$Q_S = F_{S,z} + F_{S,bot,z} \qquad (13)$$

Where, Q_S is the shaft resisting force, and $F_{S,bot,z}$ is the vertical force at the shaft bottom surface. During retraction, the force criterion *C9* (Eq. 14) check for the sufficiency of tip anchor needs to be fulfilled:

$$F_{TA} \geq Q_S \qquad (14)$$

VI. Tip Contraction (TC)

The tip is contracted with a constant velocity v_{TC} to its original size, as defined in the criterion *C10*. Similarly, the tip contraction requires a smaller force compared with tip expansion. So, the contraction rate can be faster (Table 5).

3 Efficient configurations for self-burrowing

This section attempts to identify appropriate parameters and configurations to produce efficient self-burrowing behaviours. Particular attention is paid to the shaft expansion, tip penetration, tip expansion and shaft retraction steps, while the shaft and tip contraction steps are not evaluated since they appear to be feasible in a wider range of conditions.

3.1 Preparation actions before self-burrowing

Razor clams can initiate burrowing from ground surface taking advantage of their flexible foot. This initial embedment is modelled by an initial embedment of the probe into the soil with a constant velocity v_p of 40 cm/s until the tip reaches a depth of 34 cm, at which the entire probe is fully embedded. Figure 7 shows the evolution of Q_T and Q_S against the penetration depth h. Q_T increases almost linearly with h due to gravitational pressure gradient, and the particle displacements show a shallow failure of the soil. The maximum value of Q_T is 2.19 kN at the depth of 34 cm, which could be used as a reference value for tip penetration. After reaching the target depth, a servo control mechanism was enabled to allow the probe to equilibrate under its own weight by solving Newton's second law. During this stage, Q_T

decreases rapidly to almost zero due to very slight upward movement and finally an equilibrium state between the probe self-weight and soil resisting forces was attained. At this point, the model was deemed to be in an appropriate state for launching self-burrowing cycles.

3.2 Shaft expansion: target force determination

After the initial penetration, the shaft is expanded to reach a target radial force $F_{S,r,target}$ that has to be sufficient for subsequent tip penetration. This target force needs to be determined and assigned before shaft expansion. After determining a target force, the ILC algorithm is used for reaching the target force determined based on the initial penetration resistance during shaft expansion. First, this target force strategy, as described in section 3.1, is evaluated. Then, $F_{S,r,target}$ is determined using an alternate strategy based on the maximum normal force that can be mobilized by the anchor.

Shaft expansion has been shown to reduce the tip penetration resistance (i.e., Chen et al. 2021); however, a conservative assumption to ensure the sufficiency of radial normal shaft force to enable tip penetration is to use the maximum resisting force Q_T recorded during the initial penetration phase (Figure 7) and the shaft's friction coefficient μ_p to calculate $F_{S,r,target}$. The relevant expression is given as:

$$F_{S,r,target} = \frac{Q_T}{\mu_p} \quad (15)$$

Taking Q_T =2.19 kN and μ_p =0.35 into Eq. (15), the value of $F_{S,r,target}$ is 6.25 kN. Following the ILC algorithm, a loading increment $F_{S,r,inc}$ of 200 N was adopted to gradually approach $F_{S,r,target}$, as shown in Figure 8a. While the shaft expansion terminated after meeting the C2 criterion with an ER_S =50%, only about 2 kN of force was mobilized, which is significantly smaller than the calculated $F_{S,r,target}$ of 6.25 kN. It is also observed from the velocity profile in Figure 88b that the expansion velocity of the anchor outer surface $v_{S,r}$ is relatively large at the termination point. In addition, it takes longer to reach equilibrium ($v_{S,r}$=0) at the loading increments close to the termination point than at initial increments, indicating continuous softening of the soil likely caused by the observed shallow passive failure. Although the strategy is simple, the soil surrounding the anchor cannot mobilize the required resistance.

An alternate strategy for determining $F_{S,r,target}$ is to use the maximum normal anchorage force that can be mobilized. To estimate the soil strength around the shaft before expansion, solutions such as cavity expansion theory can be used. Here benefiting from the created DEM model, a loading algorithm with constant velocity (CV) was used as a simple way to determine $F_{S,r,target}$.

During CV expansion, the shaft radius increases with a constant rate of 0.02 m/s, interacting quasi-statically with the surrounding particles. As shown in Figure 9, the shaft radial force during CV expansion gradually increases to a peak value. This peak value can thus be used as $F_{S,r,target}$ considering a reduction factor of 0.8 (i.e. factor of safety of 1.25), leading to an $F_{S,r,target}$ of 1.6 kN. The ILC algorithm was again used with an increment of 200 N to reach the target force, which was achieved with only 17.6% of ER_S (Figure 9). This target force determination strategy was used for shaft expansion in the self-burrowing simulations presented in section 4 due to its satisfactory performance.

3.3 Tip penetration strategies

3.3.1 Quasi-static penetration

The SE stage is followed by tip penetration. We first try using Quasi-Static Penetration (QSP) in which the tip is simply pushed with a constant rate of 0.05 m/s. The quasi-static condition of the system was ensured by satisfying the inertial number upper bound ($<10^{-2}$) for quasi-static conditions, and the inertial number in the system was calculated following Ciantia et al. (2019). QSP was conducted under two shaft control strategies (CR and CF) as mentioned in section 2.2.2. Figure 10 shows the force against penetration depth obtained from the two shaft control strategies. Tip resisting force Q_T rapidly rises to meet the C3 criterion after a negligible penetration distance, i.e., 0.05 cm for CR condition and 0.06 cm for CF condition. Therefore, an effective approach to reduce tip resistance is needed to increase the penetration distance.

3.3.2 Implementation of tip oscillation in penetration

To reduce locomotion resistance in the development of a soft robot, Ortiz et al. (2019) employed bi-directional head oscillation strategy inspired by *Polychaeta*, which allowed it to achieve longer locomotion distance. In this study, we adopt a similar oscillation strategy for the tip cone that occurs simultaneously with downward penetration. The oscillation algorithm is illustrated in Figure 11. The cone tip point oscillates horizontally to the right and left in planar movement with the velocity of v_{TO} in each oscillation cycle time t_I. At $t = 0.25t_I$ and 0.75 t_I the tip point reaches the far right and the far left, respectively, while at $t = 0.5t_I$ and t_I the tip point returns to the original middle position. Stress concentration occurs around the tip during oscillation as illustrated by the contact force network in Figure 11. Note that only vertical forces are checked via the criteria described in section 2.2.2, while the real torque balance resulting from tip oscillation is not considered because the probe shaft is fixed.

The vertical penetration velocity v_p and the two parameters defining oscillation (v_{TO} and t_I) are controlling parameters that can be adjusted to optimize tip penetration. We explored various sets of parameters combining different values. Eventually, values of v_p= 0.05 m/s, t_I=0.1 s and v_{TO} = 0.8 m/s were chosen for this study due to their sufficient performance in enabling tip advance. The oscillation amplitude ($0.25\times v_{TO}\times t_1$) is 2 cm, similar to the probe radius 1.78 cm. The CF shaft control was employed to maintain the shaft normal force. Without violating the *C3* force criterion, the tip advances 2 cm (Figure 12a) until the *C2* ER_S limit is triggered (Figure 12b). Then, the probe oscillates back to the middle position to terminate tip penetration.

3.4 Tip expansion strategy

The soil around the tip is able to provide more resistance at greater depths than the shaft. Therefore, the target force of tip expansion $F_{Tcyl,r,target}$ is determined from the recorded shaft friction Q_S and the current value of Q_T since they both act in an upward direction, as described:

$$F_{Tcyl,r,target} = \frac{Q_S+Q_T}{\mu_p} \tag{16}$$

Taking Q_S as 0.6 kN which is three times the maximum Q_S recorded in Figure 7 and the value of Q_T as 0.12 kN from the termination point of tip penetration into Eq. (16), the value of $F_{Tcyl,r,target}$ was calculated as 2.0 kN. The incremental load control algorithm was used to gradually reach the target force. Figure 13 shows the loading stages of tip radial force and tip radial expansion velocity against tip expansion magnitude (ER_T). The target force was attained at ER_T of 25.7%, indicating a satisfactory performance of the target force determination strategy.

3.5 Shaft retraction strategy

The shaft contracts back to its original diameter with v_{SC} = -0.1 m/s after tip expansion. Then, the shaft was dragged down with v_{SR} = -0.1 m/s doubling the TP velocity to recover the neck extension attained in TP. Figure 14 shows the evolution of F_{TA} and Q_S against retraction distance $\Delta\rho_{shaft}$. Without violating the force criterion *C9*, the retraction distance reaches 2 cm, which is equal to the distance achieved during TP. This full recovery proves that the tip anchor is able to provide enough reaction force to overcome the force resisting shaft retraction. The evolution of F_{TA} is relatively stable indicating less notable influence from the retraction action, while Q_S presents more oscillations due to particle rearrangements triggered by the shaft retraction. Interestingly, $F_{S,z}$ and $F_{S,bot,z}$, as the two components of Q_S, appear to be nearly identical during the whole process of retraction. Explanations of this phenomenon are provided in section 4.1 with contact force visualizations. After retraction, the tip is contracted with v_{TC} = -0.1 m/s to its original diameter, after which a new cycle can initiate.

3.6 Summary of simulation configurations

Table 5 summarizes the key parameters used in each stage of the self-burrowing simulations and the corresponding results. According to the trials presented above, an initial self-burrowing cycle can be completed from where more cycles can be performed to burrow deeper into the soil as is presented later.

4 Self-burrowing with a dual-anchor probe

4.1 One complete self-burrowing cycle

Significant interactions between the three force variables can be observed throughout the burrowing cycle, as shown in the evolution of three representative force variables Q_T, $F_{S,r}$, and $F_{Tcyl,r}$ presented in Figure 15a. The interactions between the shaft and tip during the SE and TP stages as reported by Chen et al. (2021) and Chen et al. (2022) are not clear in these simulations due to the constant normal force algorithm used to control the shaft expansion. However, the following interactions take place:

- TE: when the tip expands to a target $F_{Tcyl,r}$, the shaft radial force $F_{S,r}$ decreases dramatically.
- SC: when the shaft contracts, $F_{S,r}$ drops to near zero, causing $F_{Tcyl,r}$ to also reduce significantly.

With the implementation of tip oscillation, the tip could eventually advance 2 cm, which was then fully recovered through shaft retraction. This is shown in the evolution of the shaft and tip displacement measured during one complete self-burrowing cycle presented in Figure 15b.

Figure 16 shows the development of both the contact force network and displacement field at the end of steps I-VI. The left and right side of each image presents contact force and particle displacement, respectively. The presented particle displacements are accumulated from the beginning of the first step in the self-burrowing cycle (step I) and only displacements above a certain value of 0.1 mm are shown in the images. These images present important micromechanical observations in each step:

I: SE. The contact force is mainly concentrated at the shaft, particularly at the area near the neck. This is due to the concentration of contact forces around the probe induced during initial penetration and to the gravity-induced stress gradient in the specimen. The uniform shaft expansion can be reflected from the relatively uniform distribution of particle displacement along the shaft. The displacement field shows a passive soil wedge that propagates to the free surface due to the shallow embedment.

II: TP. During this step, the tip advances into the soil while the tip oscillates horizontally and the normal force is maintained on the shaft. To maintain the shaft force, the shaft expands continuously with a relatively slow rate, leading to a more uniform distribution of contact force and greater particle displacements along the shaft.

III: TE. The contact force concentration shifts from locations near the shaft to locations around the tip. The contact forces along the shaft become less notable compared to the previous steps. Correspondingly, the particles around the tip anchor displace radially as the target anchorage force is mobilized.

IV: SC. The shaft contraction leads to a decrease of the contact forces around the shaft and the tip. The particle displacement mobilized during shaft expansion is now recovered to a certain extent.

V: SR. During shaft retraction, the contact forces around the tip barely change, while contact force concentration appears at the bottom of the shaft with an angle of 45° because of the equal magnitudes of $F_{S,z}$ and $F_{S,bot,z}$ as shown in Figure 14.

VI: TC. After tip contraction, the contact force network shows smaller magnitudes along the entire probe length compared with Figure 7c, indicating a relaxation effect of the self-burrowing behaviors on the contacts between surrounding soil particles.

4.2 Work done during self-burrowing

Comparing the work done during each of the self-burrowing steps can shed light on the soil-probe interactions. Zhang et al. (2021) validated the computation correctness of energy components involved in DEM simulations of the standard penetration test (SPT) in virtual calibration chambers. In this study, we extend this strategy to quantify the work during each simulation stage.

The work done by shaft expansion, W_{SE}, can be calculated by time-integrating the product of the absolute magnitude of the shaft radial force with the expansion velocity, as follows:

$$W_{SE} = \int \left| F_{S,r}(t) v_{S,r}(t) \right| dt \qquad (17)$$

During TP, both tip penetration and oscillation require work. The work done by tip penetration, W_{TP}, can be calculated by time-integrating the product of the absolute Q_T magnitude with the penetration velocity:

$$W_{TP} = \int \left| Q_T(t) v_p(t) \right| dt \qquad (18)$$

The work done by tip oscillation, W_{TO}, can be computed by time-integrating the product of the absolute magnitude of tip cone force along x-axis, $F_{Tcone,x}$, with the average tip oscillation velocity:

$$W_{TO} = \int \left| F_{Tcone,x}(t) v_{TO}(t)/2 \right| dt \qquad (19)$$

The work contributed by the tip cylinder expansion, W_{TE}, is computed by time-integrating the product of the absolute radial force magnitude at the tip cylinder with the expansion velocity:

$$W_{TE} = \int \left| F_{Tcyl,r}(t) v_{Tcyl,r}(t) \right| dt \qquad (20)$$

The work done by shaft retraction, W_{SR}, can be computed considering the contribution of both the vertical force components $F_{S,z}$ and $F_{S,bot,z}$, as follows:

$$W_{SR} = \int \left(\left| F_{S,z}(t) v_p(t) \right| + \left| F_{S,bot,z}(t) v_p(t) \right| \right) dt \qquad (21)$$

The work done by shaft contraction W_{SC} and the work done by tip contraction W_{TC} can be calculated using Eq. 17 and Eq. 20, respectively.

The evolution of the work components during one self-burrowing cycle is presented in Figure 17. Shaft contraction, shaft retraction and tip contraction result in a negligible amount of work, so these three components are not included in Figure 17. The total work summing up all the work items is termed as W_{tot} and its evolution to the final value of 60 J is also plotted. Surprisingly, the most work is done by tip oscillation with more than 50% of the total work, while tip penetration only does a relatively small amount of work of 5%. To maintain constant shaft force, the shaft does more work during the TP stage than during the SE stage. Tip expansion does 12.3 % of the total work, which is also more than the initial shaft expansion.

4.3 Assessment of multiple cycles

The self-burrowing cycle was repeated three times to achieve a deeper penetration into the soil. The parameters listed in Table 5 for each self-burrowing step remain unchanged except for the shaft retraction velocity v_{SR} which was doubled in the second and third cycle to speed up contraction. The burrowing depth and mechanical work recorded in each of the three cycles are listed in Table 6. Figure 18a shows the displacement of the tip and shaft during the three cycles. The burrowing distance increases with the cycle number due to the increase of soil stress at greater depths which requires less shaft radial deformation to maintain the target force level. Figure 18b shows the evolution of the three representative forces during the self-burrowing cycles.

To compare the work done by constant rate penetration over the same distance, a separate simulation was carried out where the initial penetration in section 3.1 was continued to a depth of 43 cm. Figure 19 shows that the work during self-burrowing (i.e., W_{tot}) is greater than the work done during constant rate penetration, $W_{crPenet}$. The work done during the constant rate penetration increases linearly with depth, while there are energy oscillations in W_{tot} due to the tip oscillations and the expansion of the shaft and tip. The self-burrowing curve departs from the constant-rate one more and more with the cycles, due to the shaft expansions that caused three rises on the curve and tip oscillations that influenced the curve’s slope.

5 Conclusions

In this study, we present the results of DEM simulations of a bio-inspired self-burrowing probe in a chamber filled with a coarse-grained soil. A rough contact model has been selected to consider the micromechanical behavior of a silica sand in a realistic way. The contact model parameters for the sand have been calibrated to element tests on silica sand. The simulated self-burrowing cycle consists of six individual steps including shaft expansion, tip penetration, tip expansion, shaft contraction, shaft retraction, and tip contraction. During tip penetration, the tip oscillation strategy has been successfully employed to reduce penetration resistance and thus has significantly increased penetration efficiency. The simulation of the self-burrowing probe cycles reveals the following main findings:

- Force control algorithms employed in both shaft and tip expansion behaviors enable realistic soil-probe interaction.
- Quasi-static tip penetration can hardly achieve tip advancement due to exceeding soil resistance, with a maximum advancement of 0.06m. The tip oscillation strategy can increase the advancement in each burrowing cycle to minimally 2 cm.
- During tip expansion and shaft contraction, the radial force at the shaft and tip interacts significantly with each other.
- Microscale variables including particle displacement field and contact forces provide insightful particle-scale observations during one self-burrowing cycle. A passive failure wedge propagating from the shaft to ground free surface is caused by shaft expansion. The self-burrowing behavior produces a relaxation effect on contacts between surrounding soils.
- Through work computation, it is interesting to find that tip oscillation contributes more than 50% of the total work done by the entire self-burrowing stages.
- The probe can burrow deeper into the soil through continuous cycles. The burrowing distance increases with cycles due to soil pressure increase with depth. The work done through cycles is slightly greater than constant rate penetration resulted from shaft expansions and tip oscillations.

The results of the simulations can guide the construction of self-burrowing probe prototypes. A sophisticated device would still need a broad investigation to gain further understanding of the probe-soil interaction and open more possibilities in application. For example, the tip penetration with oscillations strategy can be optimized to balance the reduction of penetration resistances with limiting soil disturbance. Additionally, additional studies on the effects of soil type, density, confining stress, degree of saturation, depth and gravity magnitude on the self-burrowing performance are required for a broad understanding of the probe's self-burrowing ability.

~~Particularly, it is interesting to discuss the self-burrowing behavior in saturated sands because razor clams burrow there. In self-burrowing, the two main steps controlling the probe performance are SE and TP. In SE, there are two factors that are contradictiously affecting the expansion: the saturated unit weight of the sand is slightly greater than its dry unit weight, which then would require less expansion to reach a target expansion force; however, water as a low-viscosity material could significantly lubricate contacts of the sand grains at shallow depth, which then would require more expansion to reach the target force. Referring to a quasi-static penetration study where lower penetration resistances were observed in saturated sand than dry sand at comparably low stress levels (Kluger et al., 2021), we~~

would suppose that the later factor was dominating for shallow soils, so more expansion was required to reach the target force. In TP, the fast tip oscillation could increase pore water pressure and thus reduce effective stress, causing a reduction to tip penetration resistance; however, due to the fact that the 50% shaft expansion ratio was always triggered to terminate TP in the current study and more expansion during SE was necessary, less shaft expansion remains for TP, meaning that the final penetration distance would be smaller. In future studies, efforts are required to simulate self-burrowing in saturated sands using multi-phase pore fluid-discrete particulate modelling tools to evaluate the self-burrowing performance of the proposed probe.

Acknowledgements

The first author thanks the financial support of the Theodore von Kármán Fellowship - outgoings 2023 (GSO082) from RWTH Aachen University for promoting collaborations between the authors. This material is based upon work supported in part by the Engineering Research Center Program of the National Science Foundation under NSF Cooperative Agreement No. EEC–1449501. The second and third authors were supported by the National Science Foundation (NSF) under Award No. 1942369. Any opinions, findings, and conclusions or recommendations expressed in this material are those of the author(s) and do not necessarily reflect those of the National Science Foundation.

References

Arroyo, M., Butlanska, J., Gens, A., Calvetti, F., & Jamiolkowski, M. (2011). Cone penetration tests in a virtual calibration chamber. *Géotechnique*, *61*(6), 525–531. https://doi.org/10.1680/geot.9.P.067

Barasuol, V., Villarreal-Magaña, O. A., Sangiah, D., Frigerio, M., Baker, M., Morgan, R., … Semini, C. (2018). Highly-integrated hydraulic smart actuators and smart manifolds for high-bandwidth force control. *Frontiers Robotics AI*, *5*(JUN). https://doi.org/10.3389/frobt.2018.00051

Bengough, A. G., & Mullins, C. E. (1990). Mechanical impedance to root growth: a review of experimental techniques and root growth responses. *Journal of Soil Science*, *41*(3), 341–358. https://doi.org/10.1111/j.1365-2389.1990.tb00070.x

Borela, R., Frost, J. D., Viggiani, G., & Anselmucci, F. (2021). Earthworm-inspired robotic locomotion in sand: An experimental study with X-ray tomography. *Geotechnique Letters*, *11*(1), 66–73. https://doi.org/10.1680/jgele.20.00085

Burrall, M., Dejong, J. T., Martinez, A., & Wilson, D. W. (2021). Vertical pullout tests of orchard trees for bio-inspired engineering of anchorage and foundation systems. *Bioinspiration and Biomimetics*, *16*(1). https://doi.org/10.1088/1748-3190/abb414

Calvetti, F., Prisco, C., & Nova, R. (2015). Experimental and Numerical Analysis of Soil – Pipe

Interaction. *Journal of Geotechnical and Geoenvironmental Engineering*, *130*(12), 1292–1299. https://doi.org/10.1061/(ASCE)1090-0241(2004)130

Carotenuto, A. R., Guarracino, F., Šumbera, R., & Fraldi, M. (2020). Burrowing below ground: Interaction between soil mechanics and evolution of subterranean mammals. *Journal of the Royal Society Interface*, *17*(162). https://doi.org/10.1098/rsif.2019.0521

Chen, Y., Khosravi, A., Martinez, A., & Dejong, J. (2021). Modeling the self-penetration process of a bio-inspired probe in granular soils. *Bioinspiration and Biomimetics*, *16*(4), 46012. https://doi.org/10.1088/1748-3190/abf46e

Chen, Y., Martinez, A., & Dejong, J. (2022). DEM simulations of a bio-inspired site characterization probe with two anchors. *Acta Geotechnica*, *5*. https://doi.org/10.1007/s11440-022-01684-5

Chen, Y., Martinez, A., & DeJong, J. (2022). DEM study of the alteration of the stress state in granular media around a bio-inspired probe. *Canadian Geotechnical Journal*, *59*(10). https://doi.org/https://doi.org/10.1139/cgj-2021-0260

Ciantia, M., Arroyo, M., O'Sullivan, C., Gens, A., & Liu, T. (2019). Grading evolution and critical state in a discrete numerical model of Fontainebleau sand. *Géotechnique*, *69*(1), 1–15.

Ciantia, M. O., Boschi, K., Shire, T., & Emam, S. (2018). Numerical techniques for fast DEM large-scale model generation. *Engineering and Computational Mechanics*. https://doi.org/10.1680/jencm.18.00025

Ciantia, M. O., O'Sullivan, C., & Jardine, R. J. (2019). Pile penetration in crushable soils : Insights from micromechanical modelling. In *Proceedings of the XVII ECSMGE-2019* (pp. 298–317). https://doi.org/10.32075/17ECSMGE-2019-1111

Cundall, P. A. (1987). Distinct element models of rock and soil structure. In *Analytical and computational methods in engineering rock mechanics (ed. E. T. Brown)* (pp. 129–163). London, UK: Allen and Unwin.

De Macedo, R. B., Andò, E., Joy, S., Viggiani, G., Pal, R. K., Parker, J., & Andrade, J. E. (2021). Unearthing real-time 3D ant tunneling mechanics. *Proceedings of the National Academy of Sciences of the United States of America*, *118*(36), 1–7. https://doi.org/10.1073/pnas.2102267118

Dorgan, K. M. (2015). The biomechanics of burrowing and boring. *Journal of Experimental Biology*, *218*(2), 176–183. https://doi.org/10.1242/jeb.086983

Frost, J. D., Martinez, A., Mallett, S. D., Roozbahani, M. M., & DeJong, J. T. (2017). Intersection of Modern Soil Mechanics with Ants and Roots. In *Geotechnical Frontiers* (pp. 900–909).

Houlsby, G. T., & Withers, N. J. (1988). Analysis of the cone pressuremeter test in clay. *Geotechnique*, *38*(4), 575–587. https://doi.org/10.1680/geot.1988.38.4.575

Huang, S., & Tao, J. (2020). Modeling Clam-inspired Burrowing in Dry Sand using Cavity Expansion Theory and DEM. *Acta Geotechnica*. https://doi.org/10.1007/s11440-020-00918-8

Itasca, C. G. I. (2017). PFC — Particle Flow Code, Ver. 5.0. Minneapolis.

Kluger, M. O., Kreiter, S., Stähler, F. T., Goodarzi, M., Stanski, T., & Mörz, T. (2021). Cone penetration tests in dry and saturated Ticino sand. *Bulletin of Engineering Geology and the Environment*, *80*(5), 4079–4088. https://doi.org/10.1007/s10064-021-02156-y

Mallett, S. D., Matsumura, S., & David Frost, J. (2018). Additive manufacturing and computed tomography of bio-inspired anchorage systems. *Geotechnique Letters*, *8*(3), 219–225. https://doi.org/10.1680/jgele.18.00090

Martinez, A., Dejong, J. T., Jaeger, R. A., & Khosravi, A. (2020). Evaluation of self-penetration potential of a bio-inspired site characterization probe by cavity expansion analysis. *Canadian Geotechnical Journal*, *57*(5), 706–716. https://doi.org/10.1139/cgj-2018-0864

Martinez, Alejandro, DeJong, J., Akin, I., Aleali, A., Arson, C., Atkinson, J., … Zheng, J. (2021). Bio-inspired Geotechnical Engineering: Principles, Current Work, Opportunities and Challenges. *Géotechnique*, 1–48. https://doi.org/10.1680/jgeot.20.p.170

Martinez, Alejandro, Palumbo, S., & Todd, B. D. (2019). Bioinspiration for Anisotropic Load Transfer at Soil–Structure Interfaces. *Journal of Geotechnical and Geoenvironmental Engineering*, *145*(10), 1–14. https://doi.org/10.1061/(asce)gt.1943-5606.0002138

McDowell, G. R., Falagush, O., & Yu, H. S. (2012). A particle refinement method for simulating DEM of cone penetration testing in granular materials. *Geotechnique Letters*, *2*(7–9), 141–147. https://doi.org/10.1680/geolett.12.00036

Mickovski, S. B., Stokes, A., van Beek, R., Ghestem, M., & Fourcaud, T. (2011). Simulation of direct shear tests on rooted and non-rooted soil using finite element analysis. *Ecological Engineering*, *37*(10), 1523–1532. https://doi.org/10.1016/j.ecoleng.2011.06.001

Nardelli, V., & Coop, M. R. (2019). The experimental contact behaviour of natural sands : normal and tangential loading. *Geótechnique*, *69*(8), 672–686. https://doi.org/https://doi.org/10.1680/jgeot.17.P.167

O'Hara, K. B., & Martinez, A. (2022). Load transfer directionality of snakeskin-inspired piles during installation and pullout in sands. *Journal of Geotechnical and Geoenvironmental Engineering*. https://doi.org/10.1061/(ASCE)GT.1943-5606.0002929

Ortiz, D., Gravish, N., & Tolley, M. T. (2019). Soft Robot Actuation Strategies for Locomotion in

Granular Substrates. *IEEE Robotics and Automation Letters*, *4*(3), 2630–2636. https://doi.org/10.1109/LRA.2019.2911844

Otsubo, M., O'Sullivan, C., Hanley, K. J., & Sim, W. W. (2017). The influence of particle surface roughness on elastic stiffness and dynamic response. *Géotechnique*, *67*(5), 452–459. https://doi.org/10.1680/jgeot.16.P.050

Sharif, Y., Brown, M., Cerfontaine, B., Davidson, C., Ciantia, M., Knappett, J., … Ottolini, M. (2020). Effects of screw pile installation on installation requirements and in-service performance using the Discrete Element Method. *Canadian Geotechnical Journal*.

Tang, Y., & Tao, J. (2022). Multiscale analysis of rotational penetration in shallow dry sand and implications for self-burrowing robot design. *Acta Geotechnica*, *0123456789*. https://doi.org/10.1007/s11440-022-01492-x

Tao, J. (2021). Burrowing soft robots break new ground. *Science Robotics*, *6*(55), 1–3. https://doi.org/10.1126/scirobotics.eabj3615

Tao, J., Huang, S., & Tang, Y. (2020). SBOR: a minimalistic soft self-burrowing-out robot inspired by razor clams. *Bioinspiration & Biomimetics*, *15*(5). https://doi.org/10.1088/1748-3190/ab8754

Tao, J. J., Huang, S., & Tang, Y. (2019). Bioinspired Self-Burrowing-Out Robot in Dry Sand. *Journal of Geotechnical and Geoenvironmental Engineering*, *145*(12), 2819002. https://doi.org/10.1061/(ASCE)GT.1943-5606.0002177

Taylor, I., Lehner, K., McCaskey, E., Nirmal, N., Ozkan-Aydin, Y., Murray-Cooper, M., … Benfey, P. N. (2021). Mechanism and function of root circumnutation. *Proceedings of the National Academy of Sciences of the United States of America*, *118*(8), 1–10. https://doi.org/10.1073/pnas.2018940118

Ting, J. M., Corkum, B. T., Kauffman, C. R., & Greco, C. (1989). Discrete numerical model for soil mechanics. *Journal of Geotechnical Engineering*, *115*(3), 769–787. https://doi.org/10.1061/(ASCE)0733-9410(1989)115

Trueman, E. R. (1967). The dynamics of burrowing in Ensis (Bibalvia). In *Proceedings of the Royal Society of London. Series B, Containing papers of a Biological character. Royal Society (Great Britain)* (Vol. 166, pp. 459–476). https://doi.org/10.1098/rspb.1967.0007

Winter, V., Deits, R. L. H., Dorsch, D. S., Slocum, A. H., & Hosoi, A. E. (2014). Razor clam to RoboClam: Burrowing drag reduction mechanisms and their robotic adaptation. *Bioinspiration and Biomimetics*, *9*(3). https://doi.org/10.1088/1748-3182/9/3/036009

Zhang, N., Arroyo, M., Ciantia, M., & Gens, A. (2021). Energy balance analyses during Standard

Penetration Tests in a virtual calibration chamber. *Computers and Geotechnics*, *133*. https://doi.org/10.1016/j.compgeo.2021.104040

Zhang, N., Arroyo, M., Ciantia, M. O., Gens, A., & Butlanska, J. (2019). Standard penetration testing in a virtual calibration chamber. *Computers and Geotechnics*, *111*(3), 277–289. https://doi.org/10.1016/j.compgeo.2019.03.021

Zhang, N., Ciantia, M. O., Arroyo, M., & Gens, A. (2021). A contact model for rough crushable sand. *Soils and Foundations*, *61*(3), 798–814. https://doi.org/10.1016/j.sandf.2021.03.002

Zhong, W., Liu, H., Wang, Q., Zhang, W., Li, Y., Ding, X., & Chen, L. (2021). Investigation of the penetration characteristics of snake skin-inspired pile using DEM. *Acta Geotechnica*, *16*(6), 1849–1865. https://doi.org/10.1007/s11440-020-01132-2

Tables

Table 1 Physical properties of Fontainebleau sand (Ciantia et al., 2019).

Variable (unit)	Symbol	Value
Mean size (mm)	D_{50}	0.21
Maximum void ratio	e_{max}	0.9
Minimum void ratio	e_{min}	0.51
Specific gravity (kN/m^3)	ρ_s	2.65

Table 2 DEM contact model parameters (Zhang et al., 2021).

Element	*G /GPa*	v	μ	S_q /μm	r_1	r_2
F-sand	32	0.19	0.275	0.6	0.05	5
Probe	74	0.265	0.35	-	-	-

Table 3 Geometrical properties of the chamber.

Variable (unit)	Symbol	Value
Height (cm)	H_C	70
Diameter (cm)	D_C	70
Particle size scaling factors	n_1, n_2, n_3, n_4 and n_5	35, 53, 79, 95, 113
Number of particles	N	104,320

Table 4 Key geometrical and physical properties of the probe.

Variable (unit)	Symbol	Value
Probe total length (cm)	l_p	24.4
Cone diameter (cm)	d_c	3.56
Probe material density (kg/m^3)	ρ_p	8,050
Probe mass (kg)	m_p	2.23
Chamber / probe diameter ratio	D_C / D_T=R_d	20
Probe / particle ratio in the core	D_T / $n_1 D_{50}$=n_p	4.8

Table 5 Key parameters used in self-burrowing steps and corresponding results.

Step	Parameters	Results
I: SE	$F_{S,r,target}$ = 1.6 kN, $F_{S,r,inc}$ = 200 N	$F_{S,r,target}$ = 1.6 kN, ER_S =17.6%
II: TP	v_p= 0.05 m/s (Tip penetration) t_I=0.1 s, v_{TO} = 0.8 m/s, amplitude = 0.25× v_{TO} ×t_I= 2 cm (Tip oscillation)	$\Delta\rho_{tip}$ =2 cm
III: TE	$F_{Tcyl,r,target}$ = 2 kN	$F_{Tcyl,r,target}$ = 2 kN, ER_T =25.7%
IV: SC	v_{SC} = -0.1 m/s	D_{SA}= D_S
V: SR	v_{SR} = -0.1 m/s	$\Delta\rho_{shaft}$ = $\Delta\rho_{tip}$ =2 cm
VI: TC	v_{TC} = - 0.1 m/s	D_{TA}= d_c

Table 6 Measured data from multiple self-burrowing cycles

	1st cycle	2nd cycle	3rd cycle
Self-burrowing distance, Δρ / cm	2	3.5	4
Work, W / J	60	84	107

Figures

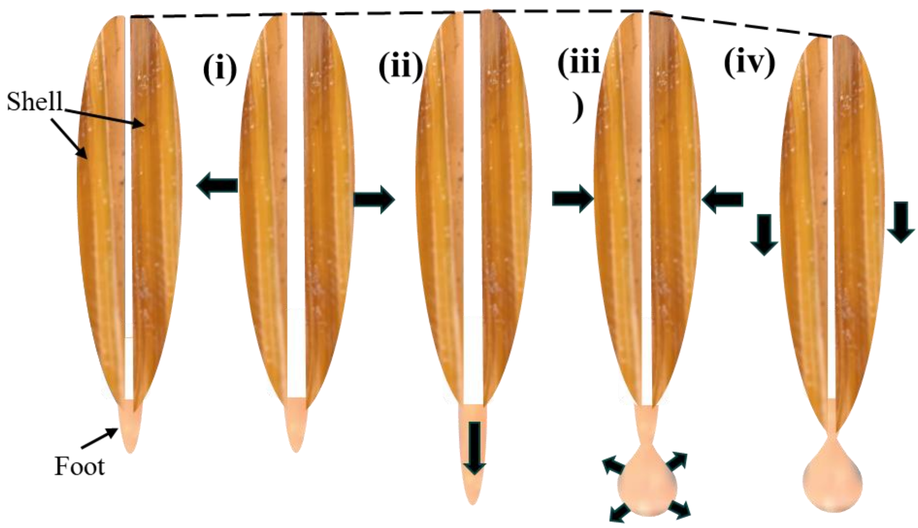

Figure 1 Typical burrowing steps of a razor clam: (i) the shell forms an anchor, (ii) the foot probes downward, (iii) the foot expands and the shell contracts, and (iv) the foot drags the shell downward. The dotted line denotes burrowing depth, and the arrows indicate movement direction of the shell and foot. Adapted from Trueman (1967) and Huang and Tao (2020).

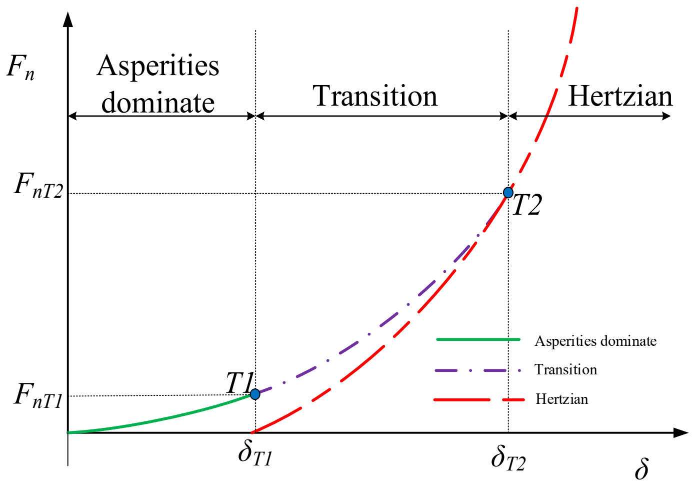

Figure 2 Schematic illustration of the rough surface contact model (after Otsubo et al., 2017).

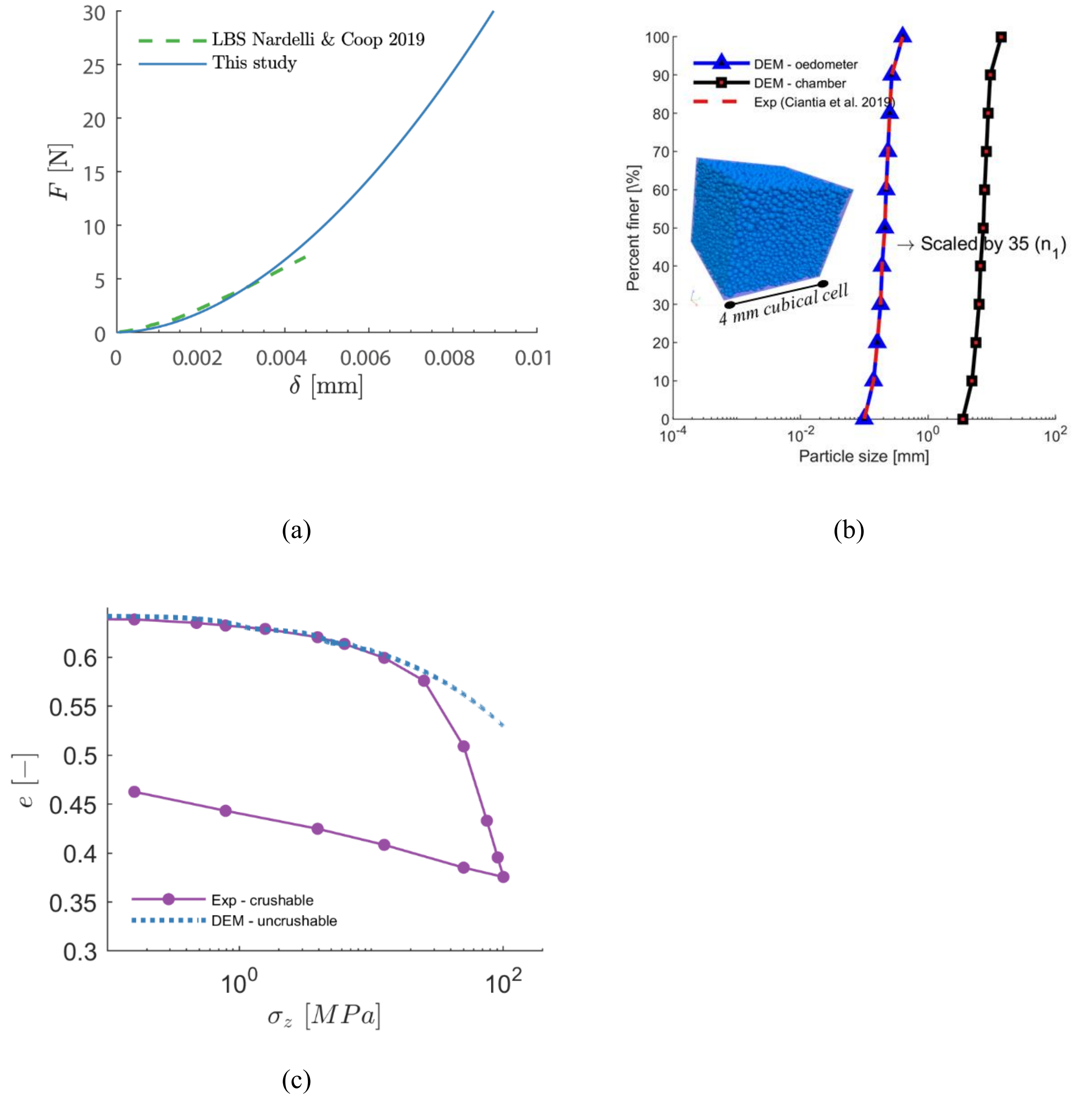

Figure 3 (a) Reproduction of load displacement curve of single grain test; (b) particle size distribution of Fontainebleau sand and DEM models for calibration; (c) reproduction of initial non-crushing loading stages of high pressure oedometric compression tests using the rough model (Zhang et al., 2021).

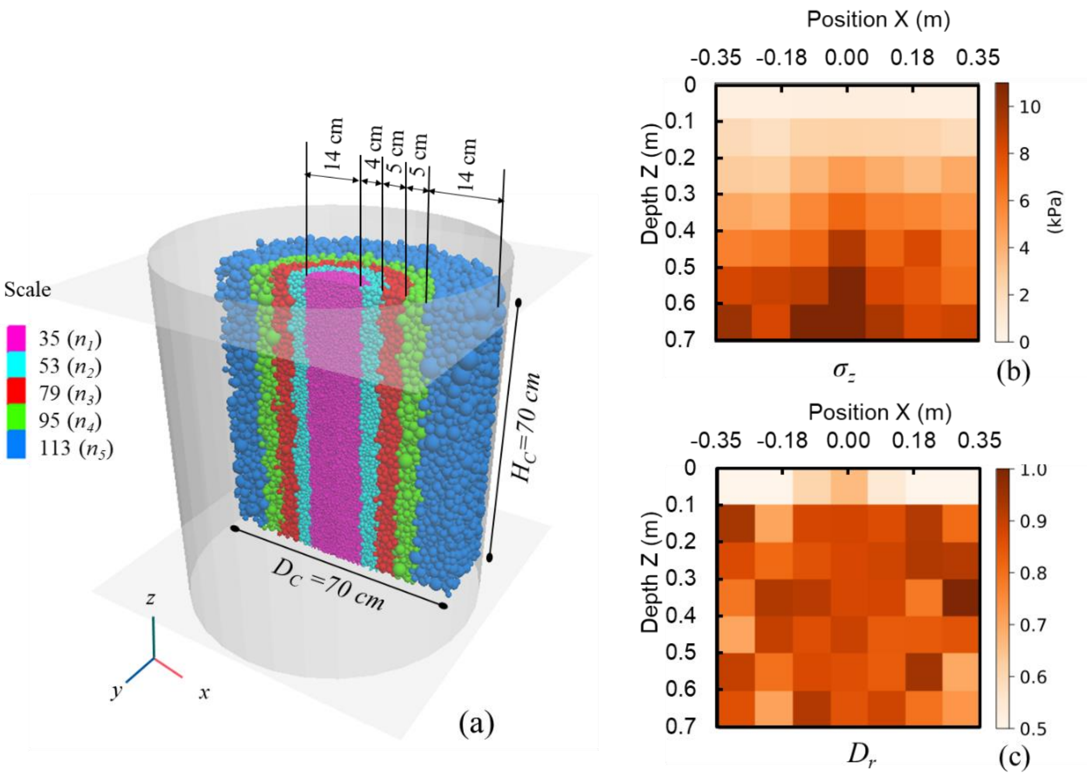

Figure 4 (a) View of DEM model with multi-upscaled particles, and sample quality check with (b) vertical stress distribution σ_z and (c) relative density D_r.

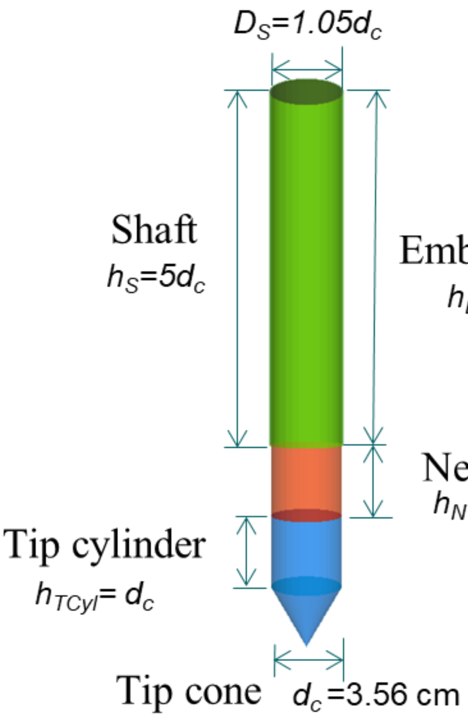

Figure 5 View of bio-inspired dual-anchor probe prototype.

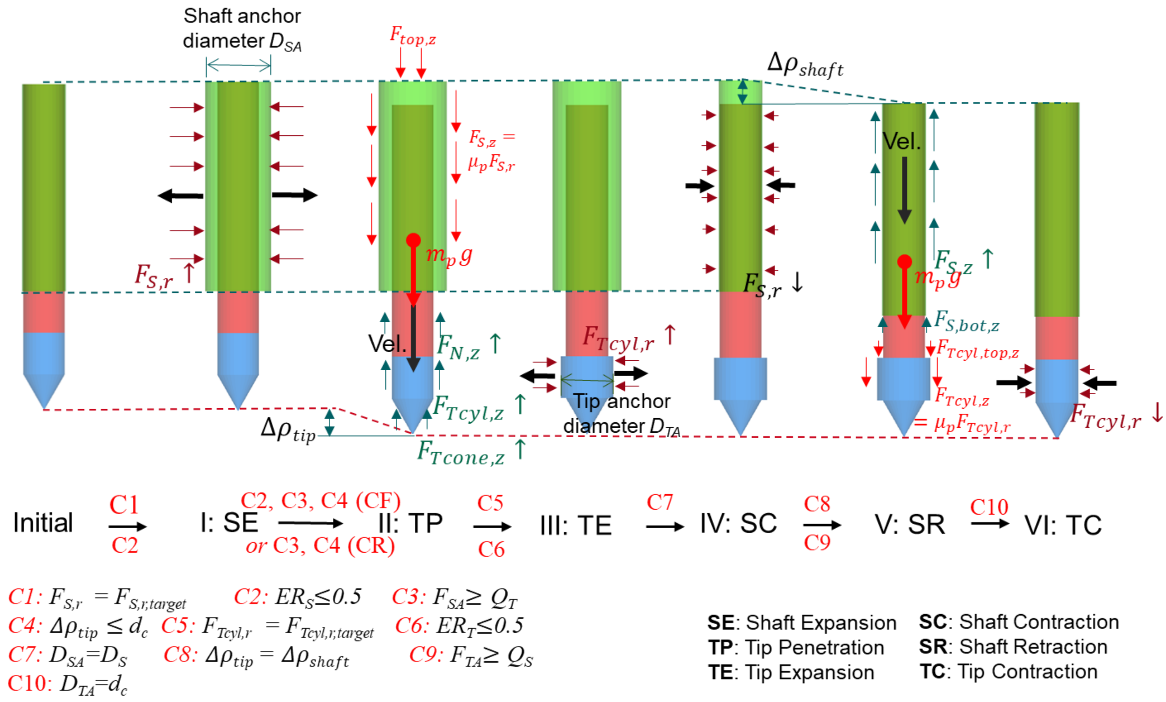

Figure 6 Schematic illustration of controlling criteria defined in each stage of one single self-burrowing cycle. Thick black arrows indicate movement direction of specific probe segments. Light blue and red arrows indicate the direction of forces. The 'up' or 'down' arrow after one force indicates increase or decrease of the force. The criteria defined in each stage present an 'OR' relation.

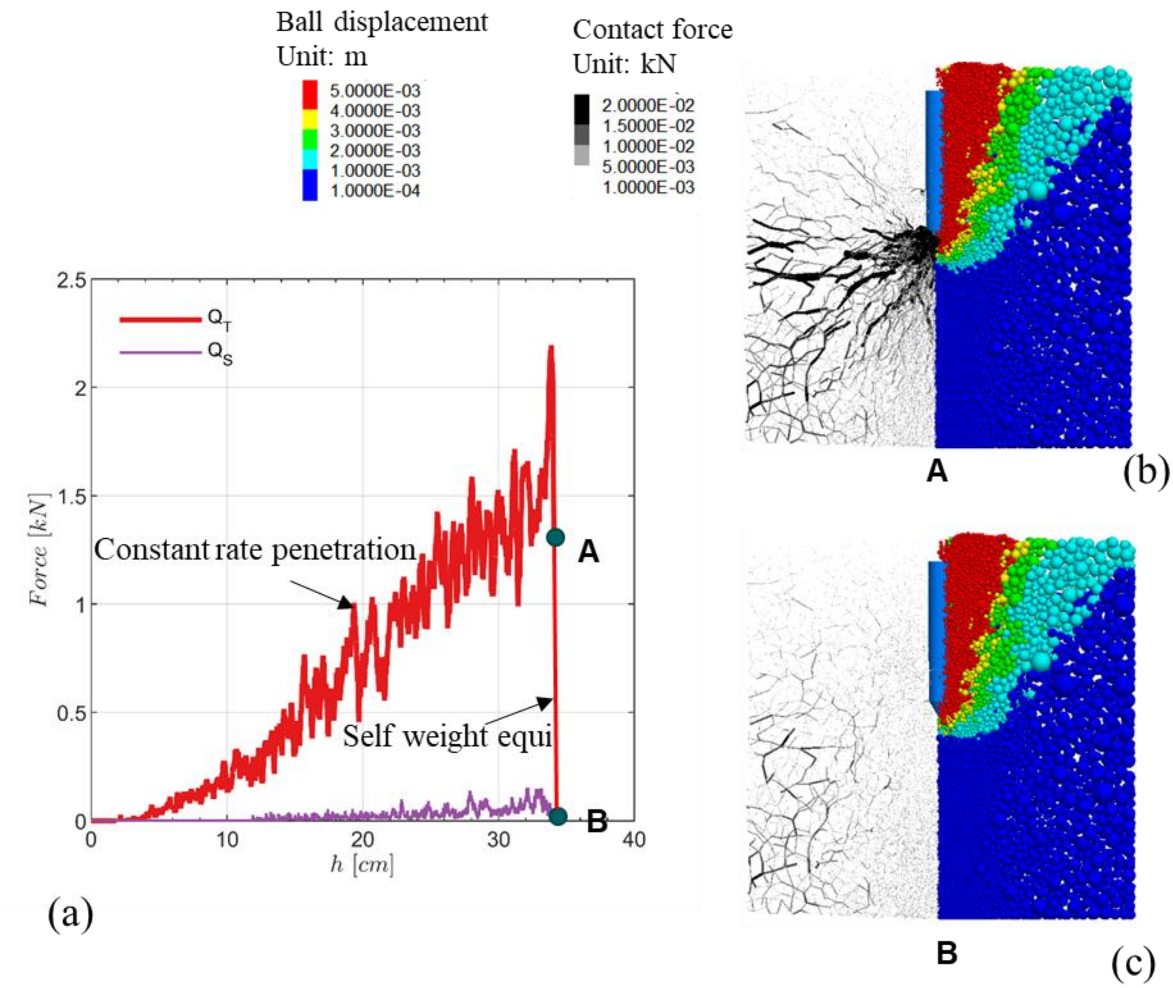

Figure 7 Preparations for self-burrowing: (a) tip resistance evolution with depth, (b) and (c) contact force (left half) and displacement field (right half) at point A and B in (a), respectively.

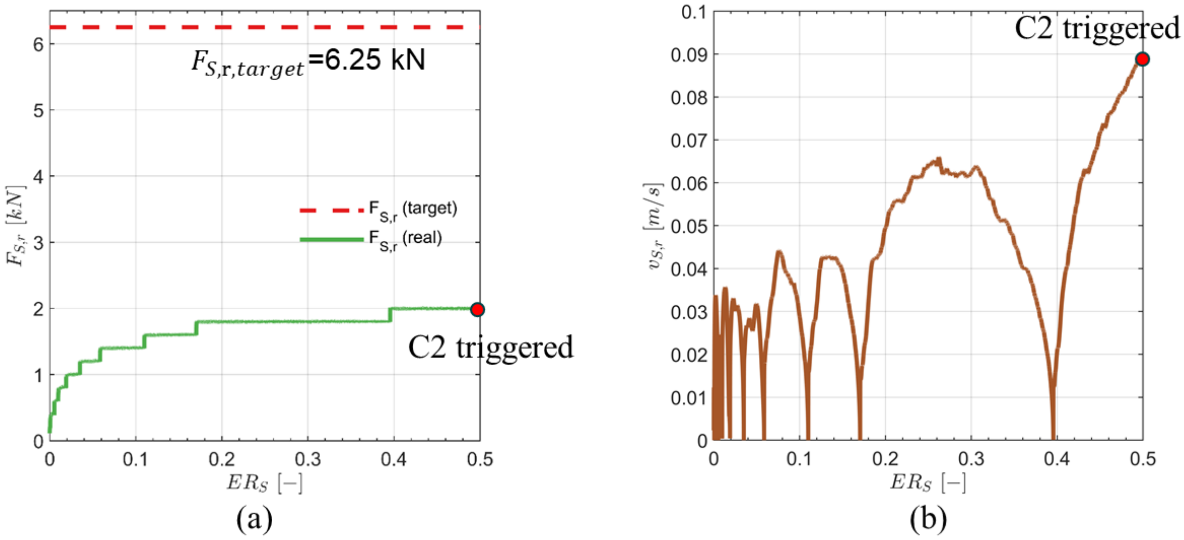

Figure 8 Loading strategy based on initial penetration resistance: (a) Radial force evolution and (b) radial velocity against shaft expansion ratio.

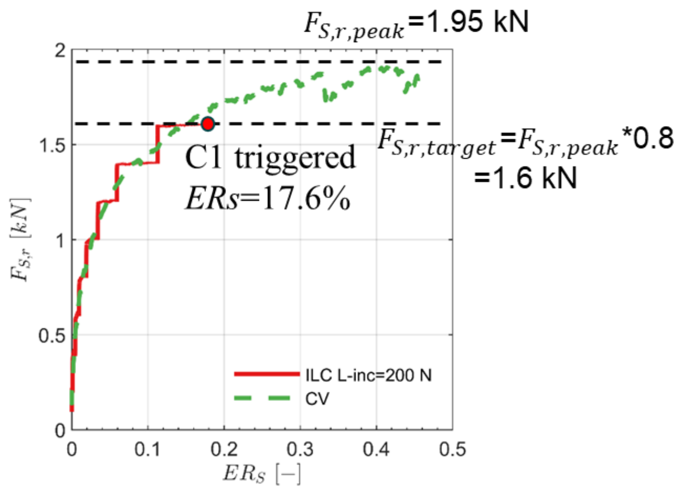

Figure 9 Shaft radial force against expansion ratio in loading strategy based on maximum anchorage force.

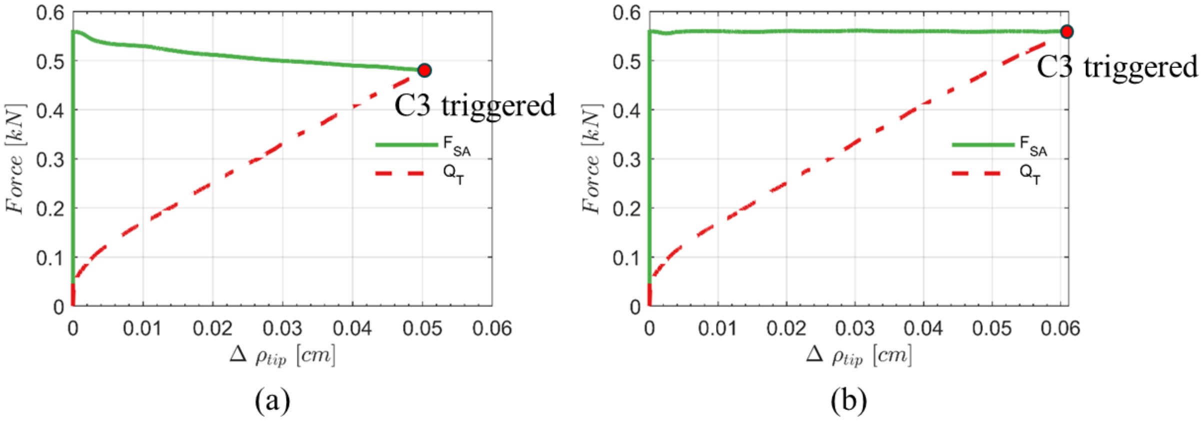

Figure 10 Force evolution against penetration depth under (a) CR and (b) CF shaft boundary condition.

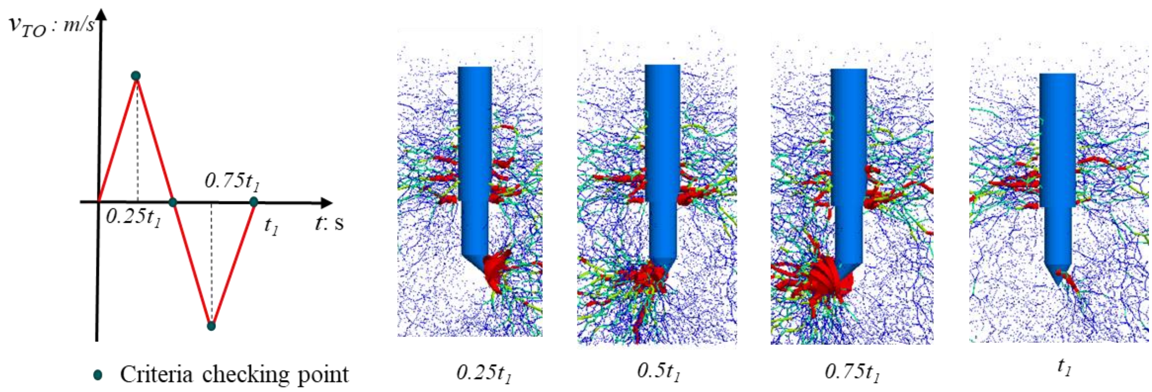

Figure 11 Tip oscillation algorithm and contact force development during oscillation. Contact force scales are the same as in Figure 7.

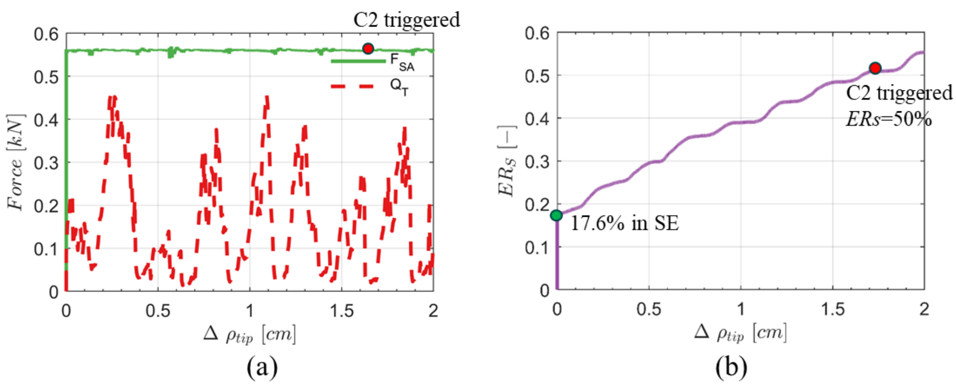

Figure 12 (a) Force evolution and (b) shaft radial expansion against penetration under CF shaft boundary condition.

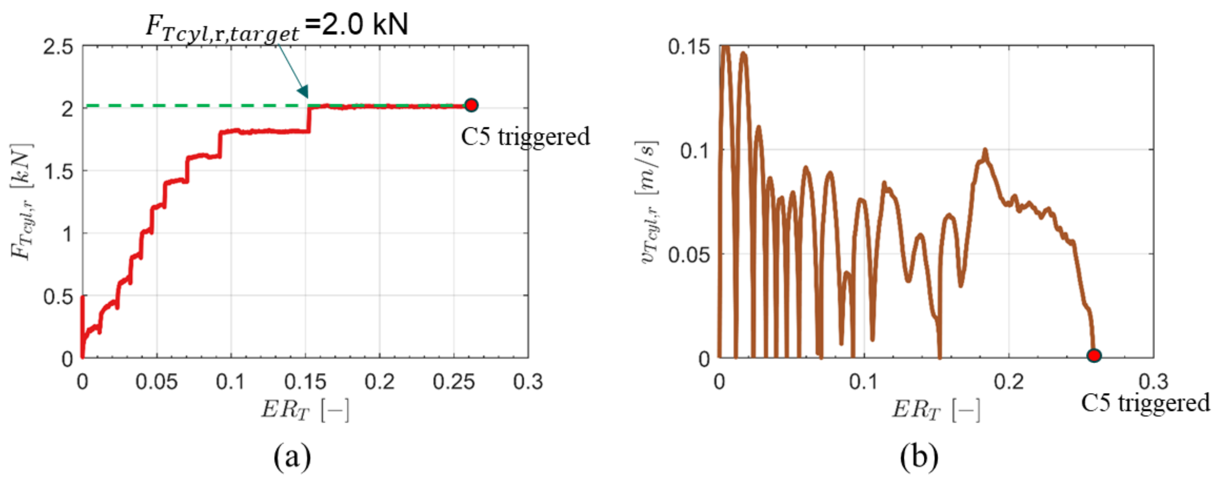

Figure 13 Incremental loading for tip expansion: (a) tip radial force and (b) radial velocity.

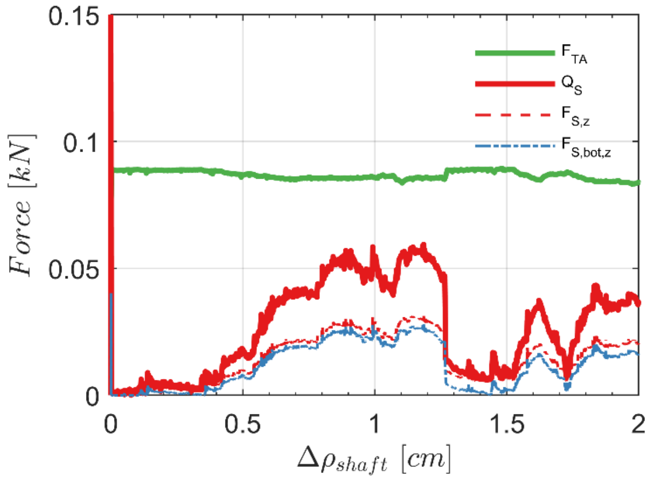

Figure 14 Evolution of relevant force elements with shaft retraction distance.

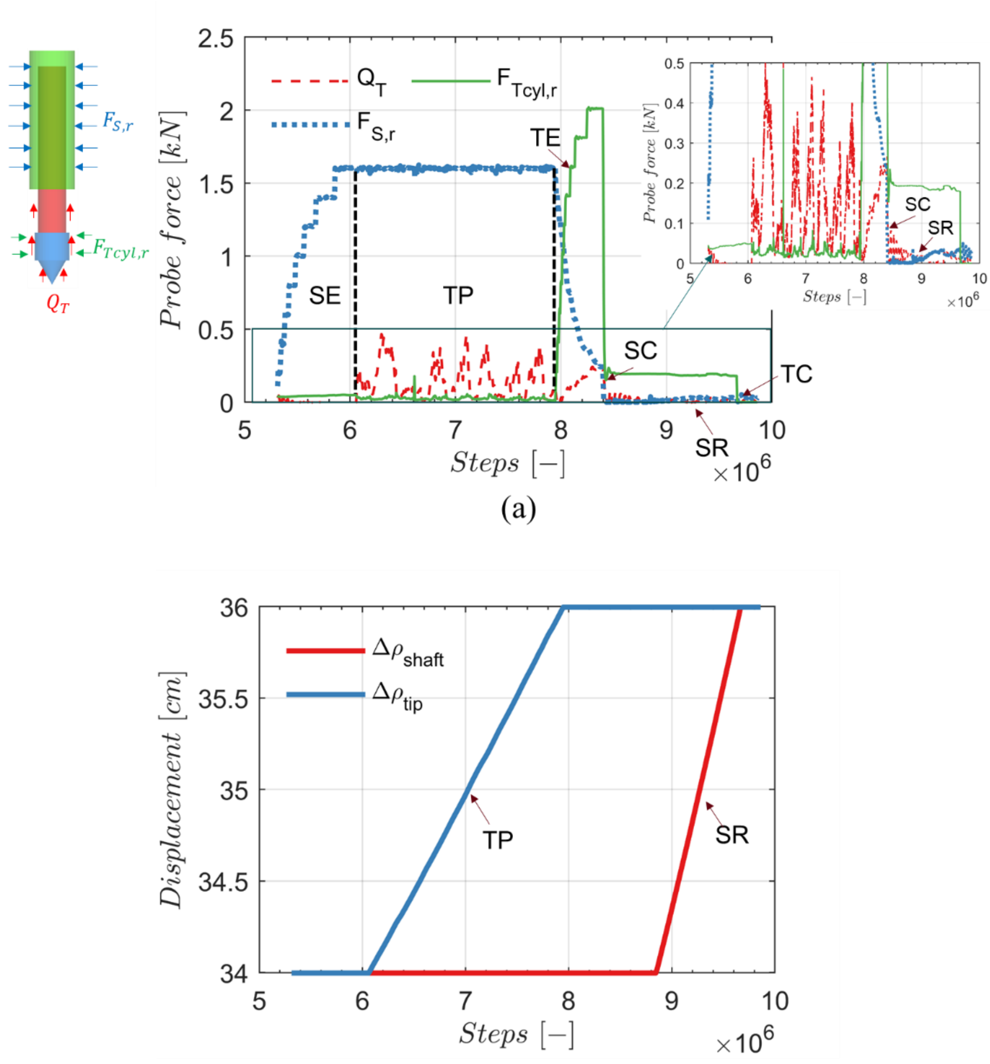

(b)

Figure 15 (a) Force evolution and (b) displacement during one single self-burroiwng cycle against numerical steps.

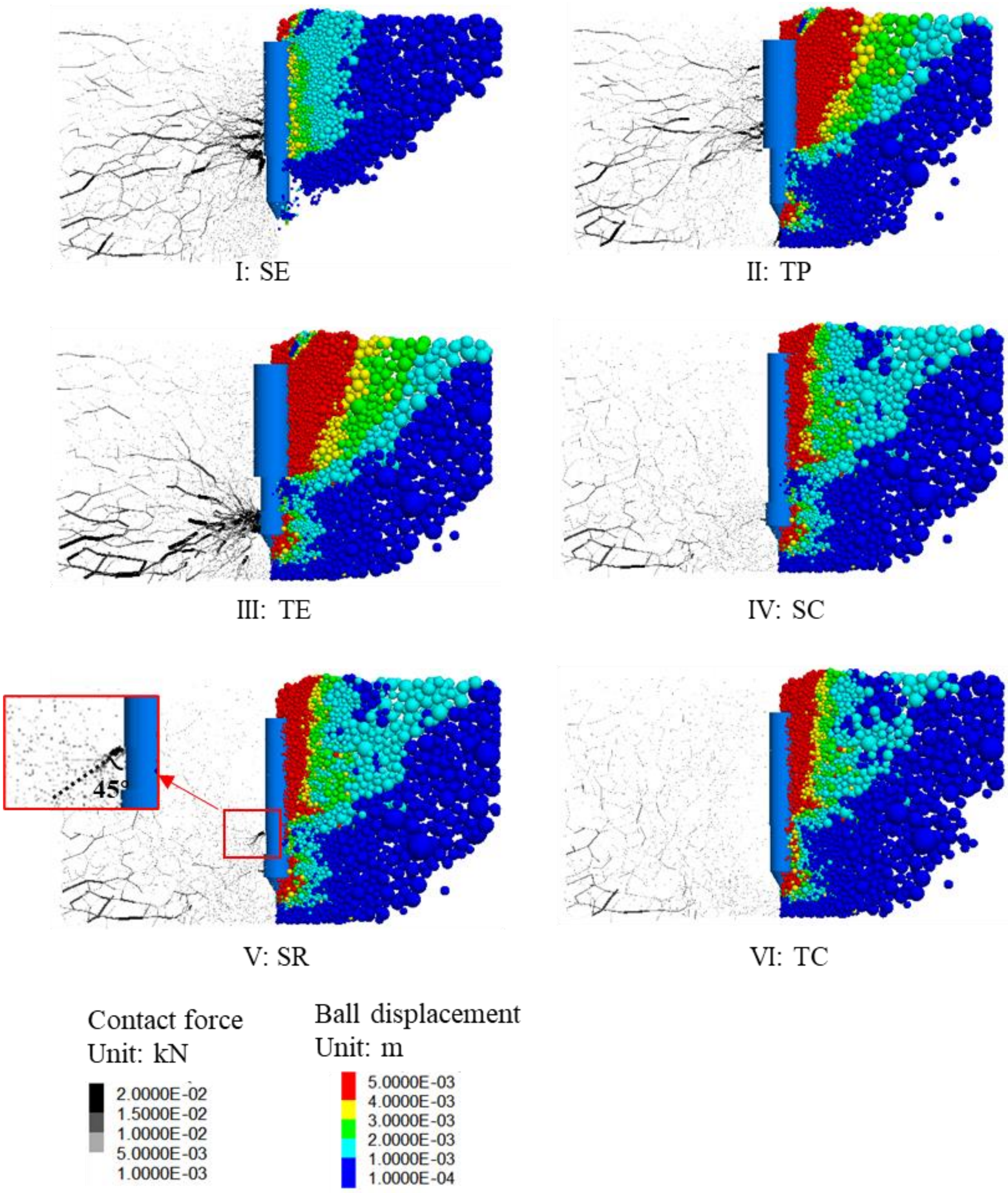

Figure 16 Micromechanical observations in each self-burrowing step. Left half of each image presents contact force network and right half presents particle displacement fields accumulated after initial penetration.

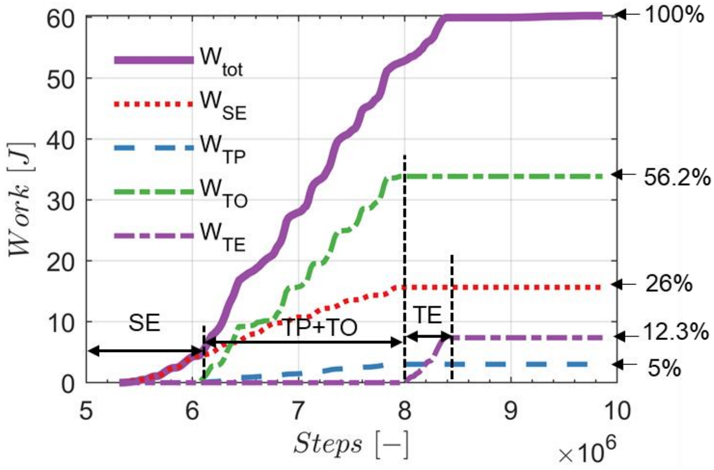

Figure 17 Evolution of work done through self-burrowing steps.

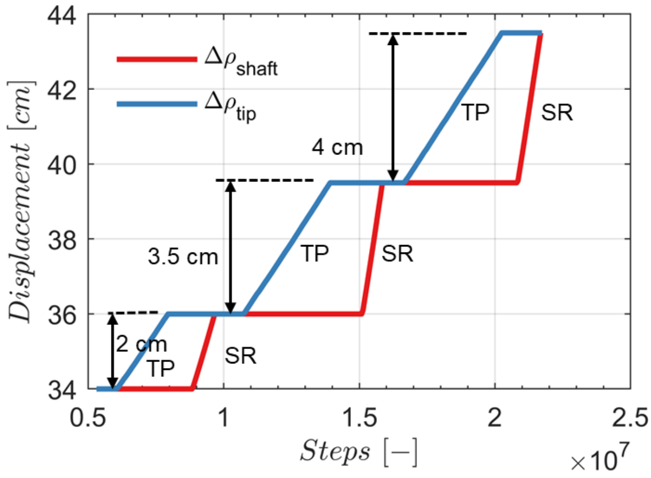

(a)

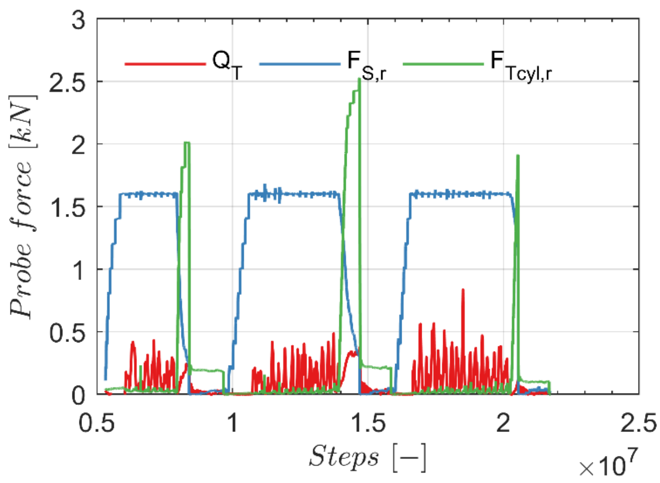

(b)

Figure 18 (a) Achieved burrowing distance and (b) measured force components during multiple cycles.

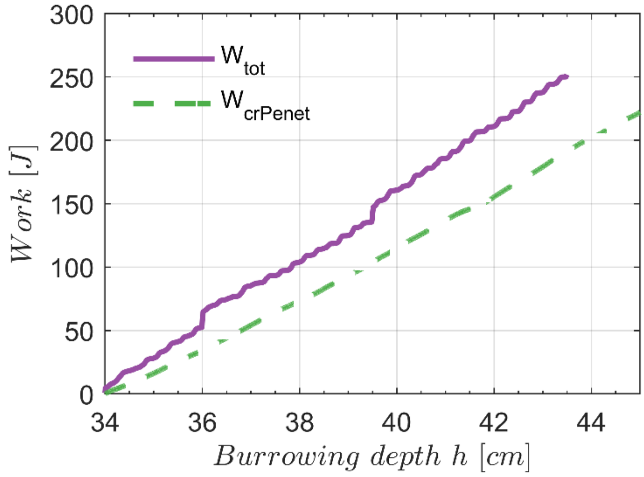

Figure 19 Energy comparisons measured in constant rate penetration and self-burrowing cycles.